Torque-Leveling Threshold-Changing Rule-Based Control for Parallel Hybrid Electric Vehicles

Article *in* IEEE Transactions on Vehicular Technology · May 2019

DOI: 10.1109/TVT.2019.2916720

2 authors:

Xuefang Li
National University of Singapore
75 PUBLICATIONS **1,021** CITATIONS
SEE PROFILE

Simos Evangelou
Imperial College London
98 PUBLICATIONS **1,515** CITATIONS
SEE PROFILE

Torque-leveling Threshold-changing Rule-based Control for Parallel Hybrid Electric Vehicles

Xuefang Li and Simos A. Evangelou

***Abstract*—A novel rule-based control strategy is proposed for the energy management of parallel hybrid electric vehicles (HEVs): the torque-leveling threshold-changing strategy (TTS). In contrast to the most commonly used heuristic electric assist control strategy (EACS) that is designed based on the load following approach, the TTS proposes and applies the new fundamental concept of torque leveling. This mechanism operates the engine with a constant torque when the engine is active, thus ensuring the engine works at an efficient operating point. The TTS additionally extends and uses a design concept that has previously been proposed in the context of series HEVs, the threshold-changing mechanism, to operate the HEV in a charge-sustaining manner. By exploiting this new set of design principles for parallel HEVs, the TTS realizes energy source control sharing behavior that is reminiscent to optimization-based methods. To show its effectiveness, the TTS is implemented to a through-the-road (TTR) HEV and benchmarked against two conventional control strategies: Dynamic Programming (DP) and the EACS. The results show that the TTS, despite its simplicity, is able to deliver comparable fuel economy as the global optimization approach DP and thus achieve significant improvement compared to the EACS. In addition, to facilitate real-time application, a simplified version of the TTS (STTS) is also developed, which is able to deliver similar performance as the TTS but is more simple to implement in practice.**

***Index Terms*—Energy management, heuristic control strategy, hybrid electric vehicle (HEV), supervisory control system (SCS).**

NOMENCLATURE

E_b	battery open circuit voltage
F	force
i_b	battery current
m	mass
P	power
Q	battery charge
q_f	fuel consumption rate
Q_{LHV}	lower heating value
R	resistance
R_{wheel}	vehicle wheel radius
T	torque
t_f	duration of drive cycle
u_{sf}	power share factor
v	vehicle speed
V_b	battery voltage
η	efficiency
ω	angular speed

Subscripts

b	battery	g	gearbox
d	drag	h	mechanical brake
dc	DC/DC converter	i	inverter
dm	motor dissipation	m	motor
e	engine	mt	motor transmission
efc	equivalent fuel consumption	pl	propulsion load
		r	tire resistance
eg	engine gearbox	t	transmission
em	electromagnetic	v	vehicle
f	fuel	$wheel$	vehicle wheel

ABBREVIATIONS

DP	dynamic programming
EACS	electric assist control strategy
ECMS	equivalent consumption minimization strategy
HEV	hybrid electric vehicle
ICE	internal combustion engine
OPSS	optimal primary source strategy
PFCS	power follower control strategy
PMSM	permanent magnet synchronous motor
TTS	Torque-leveling Threshold-changing Strategy
SCS	supervisory control system
SOC	state of charge
STTS	simplified TTS
TCS	thermostat control strategy
TTR	through-the-road
WLTP	worldwide harmonized light vehicles test procedure
XOS	exclusive operation strategy

I. INTRODUCTION

The transport sector is recognized as a major contributor to factors that exacerbate climate change, such as the increases of CO2 levels and consumption of the finite supply of oil. Much research is already being conducted to look for alternatives to the conventional vehicle, and hybrid electric vehicles (HEVs) have emerged as a viable solution. A HEV commonly combines a conventional internal combustion engine (ICE) propulsion system with a battery electric propulsion system. This type of vehicle inherits all the merits of conventional ICE vehicles and battery electric vehicles (BEVs). Compared to a BEV, the most notable advantages of a HEV are its superior mileage and flexibility in components sizing [1]. Over the past decade, the commercial success and penetration of HEVs have increased, with Toyota and Honda playing a leading role in the market.

X. Li and S. A. Evangelou are with the Department of Electrical and Electronic Engineering, Imperial College London, UK; xuefang.li@imperial.ac.uk, s.evangelou@imperial.ac.uk

This research was funded by EPSRC's grant EP/N022262/1 "Green adaptive control for future interconnected vehicles" (www.g-active.uk).

Despite this success, there is a further demand to achieve higher levels of fuel economy with HEVs to increase their competitiveness, which is an ongoing challenge. Among various possible areas of improvement, the powertrain supervisory control system (SCS) offers promising prospects for further cost-effective advances that will increase the overall efficiency of HEVs, merely by algorithmic changes in how existing components in the powertain operate and interact.

In the past, various SCSs have been developed, including optimization-based and rule-based control strategies [2]–[14]. The former type of SCSs determine the power split rules between the multiple energy sources by solving a sophisticated optimization problem, while the latter type are mainly based on heuristics. In practice, due to the high computational burden and the requirement on driving cycle knowledge, the optimization-based strategies are usually used for benchmarking. In contrast, due to the simplicity in implementation, effectiveness and robustness, the rule-based strategies are much more prevalent among commercial HEVs [15]. For parallel HEVs, the electric assist control strategy (EACS) is the commonly used rule-based control strategy [16]–[18]. However, since there are many parameters to tune in the EACS, its design process is time and effort consuming.

Over the past two decades, the approaches of load following and load leveling have been extensively used in rule-based SCSs of HEVs [3], [16]–[21]. According to the principle of load following the engine power follows the load power, such as in the power follower control strategy (PFCS) and EACS [16]–[20]. In contrast, the principle of load leveling operates the engine with a constant load and uses the battery as a buffer to cover the varying loads, which is exemplified by the conventional thermostat control strategy (TCS) [22] and more recently by the optimal primary source strategy (OPSS) [2]. It is worth highlighting that the load leveling method is more appropriate to the series HEV architecture since it is able to operate the engine-generator set continuously at an optimal torque-speed operating point due to the fact that there is no direct connection between the engine and vehicle wheels in this architecture. However, for parallel HEVs the engine is connected to the vehicle wheels mechanically through a gearbox, whereby the engine speed is constrained to vary according to the driving conditions and therefore the load leveling approach cannot guarantee that the engine will work efficiently.

Motivated by the above observations the new fundamental concept of 'torque leveling' is introduced in this work, which operates the engine with a constant torque, irrespective of the engine speed, and the battery is used as an equalizer to level the varying required torque, as the engine is activated. Torque-leveling is based on the fundamental idea that the engine efficiency varies much less at constant engine torque than constant engine power as the engine speed varies, as can be observed for example in engine efficiency maps. Hence it is possible to find an engine torque operating point which is near optimal for most of the engine operating speeds, even from idle speed, unlike any given constant engine power operating point which may even be infeasible at lower engine speeds, due to engine torque saturation. A precursor of this concept is found in the rudimentary approaches of [23], [24] proposed for the control parallel HEVs, in which constant and other engine torque set-points are activated by a single vehicular variable, such as vehicle speed, and which have no consideration of charge sustainability. Moreover, an approximate torque-leveling feature is found in the optimization-based equivalent consumption minimization strategy (ECMS), as will be studied in this paper.

The present work develops a further fundamental design concept for rule-based supervisory control of parallel HEV architectures, the threshold-changing mechanism, which has previously been established in the context of series HEV control, such as in the exclusive operation strategy (XOS) [3] and OPSS [2]. According to this concept, predefined power thresholds, instead of predefined states as in the case of TCS and PFCS, are used in the operating rules to achieve charge-sustaining operation. In the case of series HEVs these thresholds are only battery state of charge (SOC) dependent. However, given the dependence of the engine speed to the wheel speed in the parallel HEV architecture, the threshold-changing mechanism developed for this architecture in the present work has a more elaborate form that depends on both the SOC and engine speed. The threshold-changing idea is moreover found in the operation of the optimization-based ECMS for parallel HEVs, as will also be studied in this paper.

The two introduced fundamental design concepts of torque leveling and threshold changing are used together to yield a novel rule-based control strategy for parallel HEVs in this paper: the torque-leveling threshold-changing strategy (TTS). This strategy involves a smaller number of rules and hence parameters than the most common rule-based control approach for parallel HEVs, the EACS, and also it emulates the main features of the optimization-based ECMS which has similar performance with global optimal controllers, such as dynamic programming solutions [25] for simple models and certain other conditions. Although the proposed control strategy is applicable to all types of parallel HEVs, it is implemented in this paper to a through-the-road (TTR) HEV to demonstrate its effectiveness, where the dynamic modeling of the TTR HEV is also provided. The TTS is also benchmarked against the two conventional control strategies, DP and EACS. Finally, to facilitate real-time applications of the algorithm, a simplified version of the TTS, the STTS, is also developed.

The rest of the paper is organized as follows. Section II introduces the vehicle model and its powertrain. In Section III, the conventional DP, ECMS and EACS are described, and then the design principles of TTS and STTS are presented in Section IV. Simulation results in terms of power profiles, state of charge (SOC) and fuel economy are presented in Section V. Finally, section VI draws a conclusion of this work.

II. Powertrain Architecture and Modelling

TTR HEV, also known as sperate axle parallel HEV, belongs to the parallel category. In contrast to other parallel architectures, TTR is an alternative configuration with propulsion systems acting on sperate axles. The electric propulsion system (the secondary power source) including battery, permanent

magnet synchronous motor (PMSM), DC-DC converter, inverter and DC link is connected to the rear axle, and the ICE propulsion system (the primary power source) is employed to drive the front axle. The advantages of the TTR configuration can be summarized as: (1) low mechanical complexity since there is no need for a torque coupling device; (2) improved traction due to the four wheel drive; (3) suitable for hybridization of conventional vehicles.

The powertrain architecture of the TTR HEV is presented in Fig. 1. Contrary to this configuration, in the market there also exist some TTR HEV cases in which the motor is driving the front wheels while the ICE is powering the rear ones, such as the BMW i8 sports car. For this case, the energy management control can be performed similarly. Therefore, without loss of generality, this work will focus on the former powertrain configuration, which is the most general case. Currently, most of the TTR HEVs in the market are large family cars such as the Peugeot 3008 Hybrid4, Peugeot 508 RXH Hybrid4, Citroen DS5 Hybrid4, Volvo V60 D6, and so on. In this work, the vehicle model is constructed based on a 5-door station wagon-Peugeot 508 RXH Hybrid4 (2017).

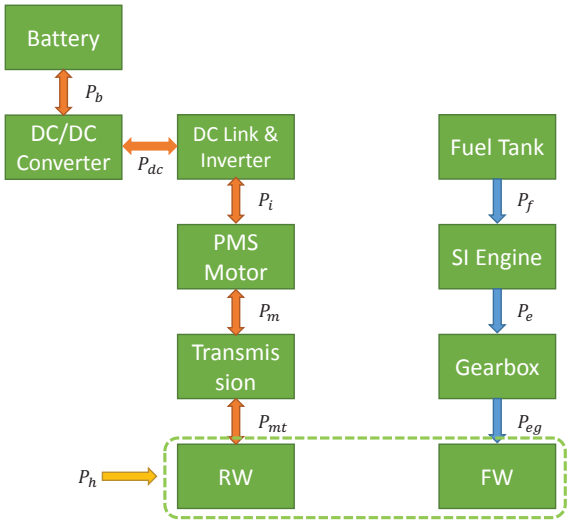

Fig. 1: Powertrain architecture of TTR HEVs.

In the TTR architecture there are five operating modes of the powertrain, which are summarized as follows: (1) the ICE alone powers the vehicle; (2) the electric motor alone drives the vehicle; (3) both the ICE and motor provide power to the vehicle; (4) the battery obtains power through regenerative braking; (5) the ICE delivers power to charge the battery through the road. By inspecting Fig. 1, it is obvious that there are three power sources that are used to drive the vehicle, including the power delivered by the primary source P_{eg}, the electric power P_{mt}, and the (mechanical) braking power P_h. P_{eg} is always non-negative, P_h is always non-positive, while P_{mt} can take any value, with negative values corresponding to either regenerative braking or battery charging by the ICE. In the present work, the mechanical braking power P_h is fixed as a proportion of the total vehicle braking power. By combining these power sources appropriately, any desired vehicle speed profile can be followed. The modeling of each powertrain component and their integration will be discussed separately in the following subsections.

A. IC engine branch (primary source)

1) IC engine: The fuel consumption dynamic of the engine can be described by

$$\frac{dm_f}{dt} = q_f(T_e, \omega_e), \tag{1}$$

in which m_f, q_f, T_e and ω_e are respectively the fuel consumed, fuel consumption rate, output torque and speed (in rad/s) of the ICE. Since in the TTR architecture the engine is mechanically connected (via a gearbox) to the wheels, knowledge of the fuel consumption rate of the engine, q_f, in terms of both the engine torque T_e and engine speed ω_e is required. In the present work, the engine map q_f is obtained from experimentally validated simulations with the widely used full CFD engine simulator, Ricardo Wave [26], for a 2L petrol engine with a peak power P_{emax} of 120 kW and a peak torque T_{emax} of 300 Nm, and presented in Fig. 2. The fuel chemical power,

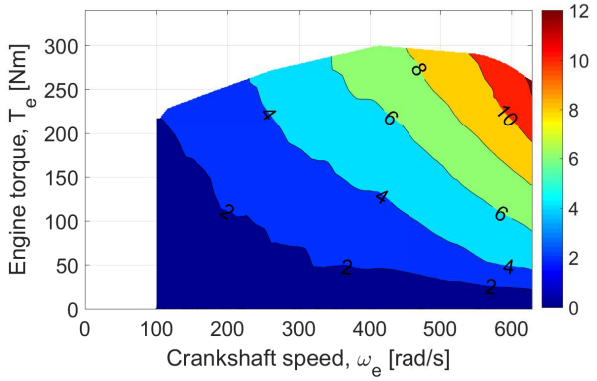

Fig. 2: ICE fuel consumption rate $q_f(T_e, \omega_e)$ in [g/s] for various engine speed and engine torque operating conditions.

$$P_f = Q_{LHV} q_f(T_e, \omega_e), \tag{2}$$

in which $Q_{LHV} = 44.4$ MJ/kg is the fuel lower heating value, is converted into mechanical power delivered by the ICE,

$$P_e = T_e \omega_e, \tag{3}$$

via the equation

$$P_e = \eta_e(T_e, \omega_e) P_f, \tag{4}$$

in which $\eta_e(T_e, \omega_e)$ is the engine efficiency. By using the $q_f(T_e, \omega_e)$ map shown in Fig. 2 and (2), (3), and (4), the engine efficiency, $\eta_e(T_e, \omega_e)$, can be derived, as shown in Fig. 3.

2) Gearbox: In this work, the model uses a 6-speed automatic transmission to connect the engine to the vehicle front axle. By using the gear ratios offered by the gearbox, the engine speed is determined by the wheel speed as follows:

$$\omega_e = g_{ei} \cdot g_{fd} \cdot \omega_{wheel}, \tag{5}$$

where g_{ei} is the ith gear ratio, g_{fd} is the final drive ratio, and ω_{wheel} is the vehicle wheel speed. The gear ratios are switched

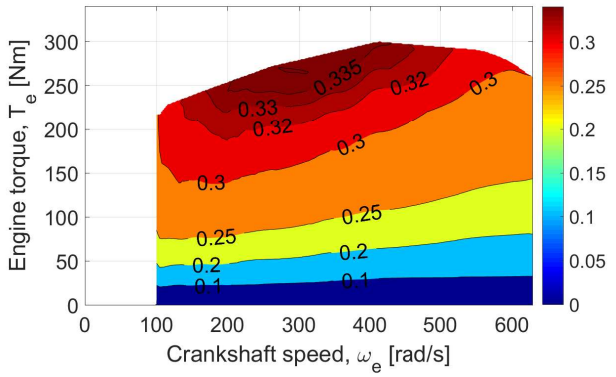

Fig. 3: ICE efficiency $\eta_e(T_e, \omega_e)$ for various engine speed and engine torque operating conditions.

TABLE I: Gear ratio values

	Gear ratio
1st gear ratio	3.54:1
2nd gear ratio	1.92:1
3rd gear ratio	1.28:1
4th gear ratio	0.91:1
5th gear ratio	0.67:1
6th gear ratio	0.53:1
Final drive ratio	4.35:1

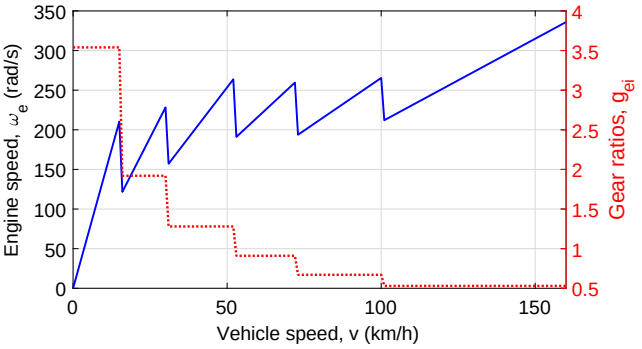

Fig. 4: Gear ratios and relationship between vehicle speed and engine speed.

according to the vehicle speed, and are given in Table I. In this work, the gear selection follows the fixed strategy shown in Fig. 4. The gearbox is assumed to have a constant efficiency of $\eta_g = 0.96$, and the power transmission is given as:

$$P_{eg} = \eta_g P_e. \tag{6}$$

B. Battery branch (secondary source)

1) Battery: The Li-ion battery model in this work is based on the battery model from the SimPowerSystems library in Simulink that has been described in [2], [27]. The battery voltage is defined by

$$V_b = E_b - R_b i_b, \tag{7}$$

where R_b is the battery internal resistance, i_b is the average current drawn from the battery, and E_b is the open circuit voltage. When the battery is discharging, E_b is described by:

$$E_b = E_0 - \frac{K_1 Q_{max}(Q_{max} - Q)}{Q} - \frac{K_2 Q_{max} i_b^*}{Q} + A_b \exp(-B_b(Q_{max} - Q)), \tag{8}$$

while the charging model is presented as follows:

$$E_b = E_0 - \frac{K_1 Q_{max}(Q_{max} - Q)}{Q} - \frac{K_2 Q_{max} i_b^*}{1.1 Q_{max} - Q} + A_b \exp(-B_b(Q_{max} - Q)), \tag{9}$$

where Q_{max} is the battery capacity, Q is the charge remaining in battery, and i_b^* is a low-pass filtered version of i_b. In the present work it is assumed that $i_b^* = i_b$. By defining the battery state of charge $SOC = Q/Q_{max}$, the battery power P_b is calculated as:

$$P_b = V_b i_b, \tag{10}$$

and therefore by using (7) and (10):

$$(E_b - R_b i_b) i_b = P_b, \tag{11}$$

where E_b is a function of SOC and i_b (as it can be seen in Eqs. (8) and (9)). By solving the symbolic equation (11), the current i_b is represented as a function of both SOC and P_b. The battery dynamic is thus described as follows:

$$\frac{dSOC}{dt} = -\frac{i_b(SOC, P_b)}{Q_{max}}. \tag{12}$$

The battery parameters are given in Table II.

TABLE II: Battery parameters

Parameter	Symbol	Li-ion Battery
Battery capacity	Q_{max}	5.65 Ah
Battery nominal voltage	E_0	230 V
Internal resistance	R_b	0.2056 Ω
Polarization constant	K_1	0.116 V/(Ah)
Polarization resistance	K_2	0.116 Ω
Exponential zone amplitude	A_b	25.1477 V
Exponential zone time constant inverse	B_b	4.2404 $(Ah)^{-1}$
Minimum battery SOC	SOC_L	50%
Maximum battery SOC	SOC_U	80%
Minimum charging power	P_{bmin}	-15 kW
Maximum discharging power	P_{bmax}	27 kW
Initial battery SOC	$SOC_{initial}$	65%

2) DC-DC converter: The battery is connected to the DC link via a bidirectional DC-DC converter that increases the battery voltage to a higher level. An average DC-DC converter model is adequate for the present purposes, such that the high frequency dynamics of the DC-DC converter are ignored and it is modeled as a static component with a constant discharging efficiency $\eta_{dc} = 0.96$. By considering the bi-directional property of the converter, the power conversion for both directions of power flow in the converter is given as follows:

$$P_{dc} = \eta_{dc}^{\text{sign}(P_{dc})} P_b, \tag{13}$$

where P_{dc} is the power that goes into the DC link.

The combined efficiency of the DC-DC converter and battery is shown in Fig. 5. It is interesting to note that the charging becomes slightly more efficient at lower SOC

levels, while discharging becomes more efficient at higher SOC levels. Therefore, if the battery is operated efficiently, charge-sustaining will indirectly take place.

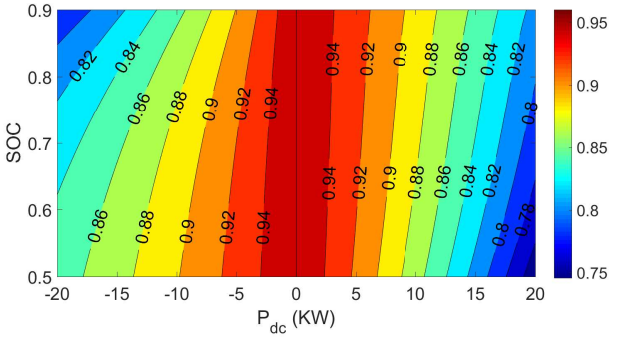

Fig. 5: Efficiency map of the secondary energy source.

3) DC link & DC-AC inverter: In this work, the battery is connected to a 700 V DC link through the DC-DC converter, and the PMSM (which drives the rear wheels) is connected to the DC link through a pulse width modulated (PWM) inverter. Similarly to the DC-DC converter, the operation of the bidirectional inverter is averaged and represented by a constant efficiency $\eta_i = 0.96$ in the associated power flow, as follows:

$$P_i = \eta_i^{\text{sign}(P_{dc})} P_{dc}, \tag{14}$$

in which P_i is the inverter output power.

4) Permanent magnet synchronous motor: This work considers a 3-phase star-connected PMSM. Its dynamics can be expressed by using the standard 2-phase rotor d-q rotating reference frame [28]–[30] as follows:

$$\frac{di_d}{dt} = (v_d - R_m i_d + p_m \omega_m L_q i_q)/L_d \tag{15}$$

$$\frac{di_q}{dt} = (v_q - R_m i_q - p_m \omega_m (L_d i_d + \lambda_m))/L_q, \tag{16}$$

where ω_m is the rotor speed, i_d and i_q are the direct and quadrature axis components of stator current, v_d and v_q are the corresponding stator voltages, L_d and L_q are stator inductances in direct and quadrature axes, R_m is the stator resistance, and p_m is the number of pole pairs per phase in the stator.

Additionally, the dynamical behavior of the rotor speed is governed by

$$J_m \frac{d\omega_m}{dt} = T_{em} + T_m + T_{dm}, \tag{17}$$

where J_m is the rotor inertia, T_m is the external load torque, T_{em} is the electromagnetic torque described as

$$T_{em} = \frac{3}{2} p_m (\lambda_m i_q + (L_d - L_q) i_d i_q), \tag{18}$$

and T_{dm} is the dissipation torque which is approximated as

$$T_{dm} = -1 - 2 \times 10^{-5} \omega_m^2.$$

to provide realistic motor efficiencies at different operating points [31], as will be shown in Figure 6.

Furthermore, the electrical power P_i and mechanical power P_m of the PMSM are given as follows:

$$P_i = \frac{3(v_q i_q + v_d i_d)}{2} \tag{19}$$

and

$$P_m = T_m \omega_m. \tag{20}$$

Due to the fast variation of the currents and much smaller magnitude of the inertia torque $J_m \frac{d\omega_m}{dt}$ as compared to the load torque T_m, the present work considers only the steady-state of the differential equations (15)-(17) and assumes that $L_d = L_q$ and $i_d = 0$; the latter condition is related to the typical control scenario in which the torque per ampere is maximized. Therefore, from (15)-(20), the electrical power can be derived as:

$$P_i = -\omega_m (T_m + T_{dm}) + \frac{2}{3} R_m \frac{(T_m + T_{dm})^2}{p_m^2 \lambda_m^2}. \tag{21}$$

The motor efficiency is thus calculated as

$$\eta_m(T_m, \omega_m) = \left(\frac{P_m}{P_i} \right)^{\text{sign}(P_i)}, \tag{22}$$

which is shown in Fig. 6 as a map that depends on T_m and ω_m and in which positive T_m corresponds to generating and negative T_m to motoring.

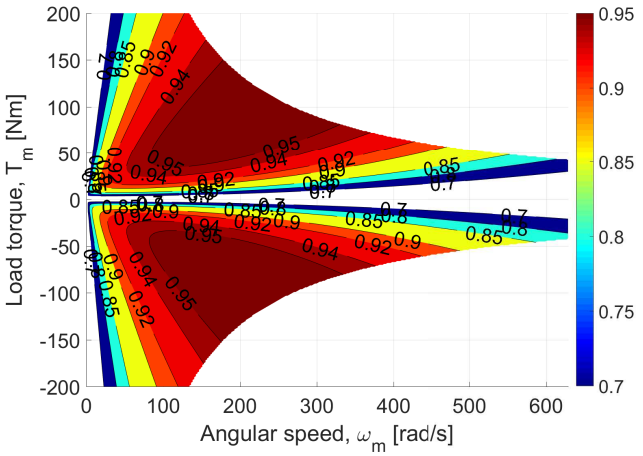

Fig. 6: Efficiency, $\eta_m(T_m, \omega_m)$, of the PMSM with load torque T_m and angular speed, ω_m.

The parameters of the PMSM are presented in Table III.

TABLE III: PMSM parameters

Parameter	Symbol	PMSM
Maximum torque	T_{mmax}	200 Nm
Maximum power	P_{mmax}	27 kW
Stator resistance	R_m	0.04 Ω
Number of pole pairs	p_m	6
Rotor magnetic flux	λ_m	0.125 Wb

5) Motor transmission: The PMSM and the vehicle rear wheels are connected by a fixed gear transmission. The relation between the angular speed ω_m of the PMSM and the vehicle wheel speed ω_{wheel} is determined by the following equation:

$$\omega_m = g_m \cdot g_{fd} \cdot \omega_{wheel}, \tag{23}$$

where g_m is a constant gear ratio and g_{fd} is the final drive ratio with the same value as in the ICE transmission. In this work, $g_m = 2.87$ is chosen. Similarly to the ICE gearbox, there are power losses in the transmission. The transmission efficiency is assumed to be $\eta_t = 0.96$, and therefore the relevant power flow can be modeled as:

$$P_{mt} = \eta_t^{\text{sign}(P_m)} P_m. \tag{24}$$

C. Vehicle model

Based on the vehicle's longitudinal dynamics, the required driving force for a given drive cycle can be calculated as follows:

$$F_v = m_v \frac{dv}{dt} + F_r + F_d, \tag{25}$$

where the vehicle speed v (≥ 0) is an exogenous input to the vehicle model determined from the driving cycle, m_v is the vehicle mass, F_r is the tire resistance force, and $F_d = \rho v^2$ is the aerodynamics drag resistance force, with ρ being the drag coefficient. In this work, m_v =1770 kg, ρ =0.47 kg/m, and F_r =70 N. Furthermore, the vehicle wheel speed is related to the vehicle forward speed by

$$\omega_{wheel} = v / R_{wheel}, \tag{26}$$

in which $R_{wheel} = 305$mm is the vehicle wheel radius. The required driving power P_{pl} is described as:

$$P_{pl} = F_v v, \tag{27}$$

which is served by the total transmission power ($P_{mt} + P_{eg} \geq 0$) and the total braking power ($P_{mt} + P_h < 0$) as follows:

$$P_{pl} = P_{eg} + P_{mt} + P_h. \tag{28}$$

The braking force distribution between front and rear axles is assumed to follow the strategy presented in Fig. 7, which is an approximation of the optimal braking performance [32]. For mild braking up to a total braking force of 5.31kN which corresponds to a deceleration of 3m/s^2 for the present vehicle model (the corner point in Fig. 7), two thirds of the braking force are on the rear axle and one third is on the front axle. When the total braking force exceeds 5.31kN, the rear axle braking force is saturated at its maximum value of 3.54 kN, while the front axle contributes the required remaining braking force. After multiplying by the vehicle speed, v, the braking force distribution can be used to determine the distribution of braking power on the front and rear axles. For the present vehicle model mechanical braking can be applied to both front and rear axles, while regenerative braking is only performed at the rear axle since it connects to the electric motor. It is further assumed that the braking power on the rear axle can be regenerated up to the battery charging power limit. According to the above assumptions, the total mechanical power P_h (on the front and/or rear axles) is given as follows:

$$P_h = \begin{cases} 0, & \forall P_{pl} \geq 0, \\ \min\{\gamma P_{pl}, P_{pl} - P_{mtmin}\}, & \forall P_{pl} < 0, \end{cases} \tag{29}$$

where $P_{mtmin} < 0$ is the minimum charging power of the secondary source, and $\gamma = 1/3$ is calculated from the braking force distribution presented in Fig. 7.

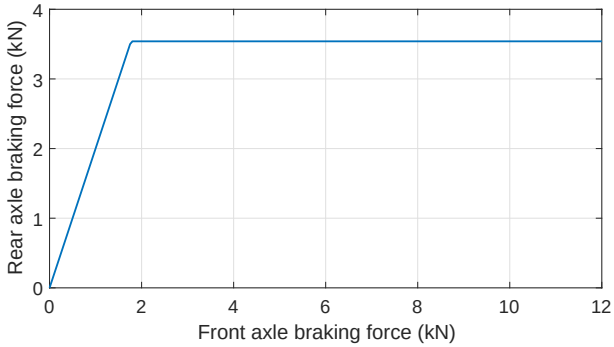

Fig. 7: Front and rear axle braking force distribution.

D. System integration

The integrated vehicle/powertrain system involves two independent power sources $\mathbf{u} = \{P_{eg}, P_{mt}\}$, which will act as the control inputs. By using the power transmission equations (2), (4), (6), (13), (14) and (24), the vehicle power flow is represented as:

$$\begin{aligned} P_e &= \eta_g^{-1} P_{eg}, \\ P_f &= Q_{LHV} q_f(T_e, \omega_e), \\ P_m &= \eta_t^{\text{sign}(-P_{mt})} P_{mt}, \\ P_i &= (\eta_m(T_m, \omega_m)\, \eta_t)^{\text{sign}(-P_{mt})} P_{mt}, \\ P_{dc} &= (\eta_i \eta_m(T_m, \omega_m)\, \eta_t)^{\text{sign}(-P_{mt})} P_{mt}, \\ P_b &= (\eta_{dc} \eta_i \eta_m(T_m, \omega_m)\, \eta_t)^{\text{sign}(-P_{mt})} P_{mt}. \end{aligned} \tag{30}$$

These equations depend on the two control inputs, P_{eg} and P_{mt}, and also on ω_e, T_e, ω_m, and T_m. By combining respectively (5)-(26), (3)-(5)-(6)-(26), (23)-(26), and (20)-(23)-(24)-(26), ω_e, T_e, ω_m, and T_m can be expressed in terms of the control inputs, P_{eg} and P_{mt}, and the exogenous input v, as follows:

$$\omega_e = \frac{g_{ei}(v) g_{fd} v}{R_{wheel}}, \qquad T_e = \frac{R_{wheel} P_{eg}}{\eta_g g_{ei}(v) g_{fd} v}, \tag{31}$$

$$\omega_m = \frac{g_m g_{fd} v}{R_{wheel}}, \qquad T_m = \frac{R_{wheel} P_{mt}}{\eta_t^{\text{sign}(-P_{mt})} g_m g_{fd} v}, \tag{32}$$

in which in the special case of $v = 0$, $T_e = T_m \triangleq 0$. The vehicle/powertrain dynamics, involving two states $\mathbf{x} = \{m_f, SOC\}$, are given as follows by collecting (1) and (12), and substituting P_b from (30) and further making use of (31)-(32):

$$\frac{d}{dt}\begin{pmatrix} m_f \\ SOC \end{pmatrix} = \begin{pmatrix} q_f(P_{eg}, v) \\ -\dfrac{i_b(SOC, P_{mt}, v)}{Q_{max}} \end{pmatrix}, \tag{33}$$

in which P_{eg} and P_{mt} are further linked by an algebraic equation given by combining (25), (27), (28) and (29).

III. Conventional Supervisory Control Systems

The main objective of the SCS is to determine the power split $\mathbf{u} = \{P_{eg}, P_{mt}\}$ between primary and secondary power sources for a given driving cycle v. $\mathbf{u}$ is free to be determined while the driving power is positive ($P_{pl} \geq 0$). When $P_{pl} < 0$, $\mathbf{u}$ is no longer free since P_{eg} becomes zero and P_{mt} is determined by (28) and (29). This section describes the design and implementation of two of the most conventional control strategies for parallel HEVs, the DP and EACS, representative of the optimization-based and heuristics-based control categories respectively. These will be used for benchmarking the new strategy in Section IV. A further optimization-based technique described in this Section, the ECMS, will be used to provide some of the insight into fundamental design principles that will be employed to develop the new rule-based control strategy.

A. Dynamic Programming

It is well-known that DP is able to provide the global optimum solution to the energy management problem for HEVs [25], although for simple vehicle models. To implement DP, the optimal control problem in the present work is formulated as follows:

$$\begin{aligned}
\min_{\mathbf{u}} \quad & m_f(t_f) && \text{(34a)}\\
\text{subject to}: \quad & \dot{\mathbf{x}} = \mathbf{f}(\mathbf{x}, \mathbf{u}) && \text{(34b)}\\
& P_{pl} = P_{eg} + P_{mt} + P_h && \text{(34c)}\\
& 0 \leq P_{eg} \leq P_{egmax} && \text{(34d)}\\
& P_{mtmin} \leq P_{mt} \leq P_{mtmax} && \text{(34e)}\\
& SOC_L \leq SOC \leq SOC_U && \text{(34f)}\\
& SOC(0) = 0.65,\ SOC(t_f) = SOC(0) && \text{(34g)}
\end{aligned}$$

where t_f denotes the duration of the given drive cycle and the dynamic model (34b) has already been specified in (33). P_{egmax} is the maximum power of the primary source, and P_{mtmin} and P_{mtmax} represent the minimum and maximum power of the secondary source respectively, where these limit values can be calculated from P_{emax}, P_{bmin}, P_{bmax} and the corresponding equations in (30). In the present work, the DP algorithm developed in [33] is implemented. As the DP solves a discrete-time optimal control problem, the engine fuel consumption dynamics (fuel mass rate) can be considered into the cost function. Therefore, for the above optimal control problem (34), the only dynamical constraint is the SOC as given in the second equation in (33). In the DP algorithm, the dynamics of SOC is discretized based on the Euler method with a sampling period of 0.1s. Furthermore, the grid points for the state and input variables are set to 501 which is reasonably large to ensure the accuracy of the simulation results.

B. Equivalent Consumption Minimization Strategy

Over the past two decades, the ECMS has been widely applied in energy management of HEVs in many variants [10]–[13]. As it has been shown in [25], the ECMS is able to achieve similar performance as DP for simple vehicle models and other simplifying assumptions, while with some loss of optimality the ECMS can also be used to benchmark against other types of energy management control strategies for complex vehicle models for which DP is unsolvable [2]. This section will mainly focus on the implementation of ECMS and explore insights informing the heuristic strategy design.

The objective of the ECMS is to minimize the equivalent fuel consumption m_{eq}, which is given as follows:

$$m_{eq} = \int_0^{t_f} q_{eq}(P_{eg}, v, P_{mt}, S_d, S_c)dt, \tag{35}$$

with

$$q_{eq} = \begin{cases} q_f(P_{eg}, v) + S_d \frac{P_{mt}}{Q_{LHV}} & P_{mt} \geq 0, \\ q_f(P_{eg}, v) + S_c \frac{P_{mt}}{Q_{LHV}} & P_{mt} < 0, \end{cases} \tag{36}$$

being the equivalent fuel consumption rate. S_d and S_c in (36) are two constant equivalence factors that translate the energy discharged/charged by the battery into a corresponding amount of fuel consumed/stored.

According to Pontryagin's minimum principle, the optimal control problem can be formulated as:

$$\begin{aligned}
\min_{\mathbf{u}} \quad & q_{eq}(P_{eg}, v, P_{mt}, S_d, S_c) && \text{(37a)}\\
\text{subject to}: \quad & \dot{\mathbf{x}} = \mathbf{f}(\mathbf{x}, \mathbf{u}) && \text{(37b)}\\
& P_{pl} = P_{eg} + P_{mt} + P_h && \text{(37c)}\\
& 0 \leq P_{eg} \leq P_{egmax} && \text{(37d)}\\
& P_{mtmin} \leq P_{mt} \leq P_{mtmax} && \text{(37e)}\\
& SOC_L \leq SOC \leq SOC_U && \text{(37f)}\\
& m_f(0) = 0,\ SOC(0) = 0.65 && \text{(37g)}
\end{aligned}$$

where the dynamic model (37b) has already been specified in (33). Therefore, for a given drive cycle v, an optimal solution of $\mathbf{u} = \{P_{eg}, P_{mt}\}$ can be obtained for each pair of equivalence factors S_d and S_c, from which an optimal power share $u_{sf} = P_{eg}/P_{pl}$ between the primary and secondary power sources can be determined. Hence, for each pair of (S_d, S_c), a control map will be generated. To obtain the optimal S_d and S_c, this process should be repeated for each candidate pair (S_d, S_c). The optimal pair of (S_d, S_c) for a driving cycle is the one that minimizes the equivalent fuel consumption m_{efc} (as defined later in Section V-C), which is obtained by an exhaustive search.

The resulting optimal control maps for four standard drive cycles, which will be defined in Section V, are shown in Fig. 8, with the corresponding equivalence factors given in Table IV. It can be seen that due to the mechanical connection between the engine and the vehicle wheels in TTR HEVs, the power sharing among the powertrain sources, u_{sf}, is determined by both the load demand, P_{pl}, and the engine speed, ω_e. Fig. 8 shows that the ICE will only be turned on when it has a high operation efficiency, for instance, when the engine operates in the region with non-blue and non-white colors in each control map. On the contrary, in the top left dark blue region of each control map, the vehicle operates with a pure electric mode, although the engine speed is high. This is because the engine operation efficiency is very low in this region which can be

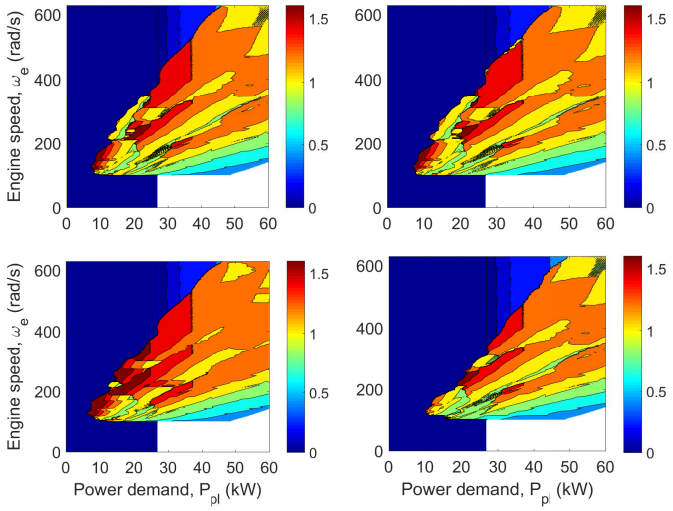

Fig. 8: ECMS control maps showing $u_{sf} = P_{eg}/P_{pl}$ for optimal S_c and S_d with WL-L, WL-M, WL-H and WL-E (respectively top left, top right, bottom left and bottom right). Dark blue corresponds to pure electric mode and white represents the infeasible region.

seen from the ICE efficiency map (engine speed ω_e against power P_e) presented in Fig. 9.

TABLE IV: Optimal equivalence factors

Driving cycle	S_d	S_c
WL-L	4.66	2.76
WL-M	4.58	2.78
WL-H	4.54	3.10
WL-E	4.06	2.62

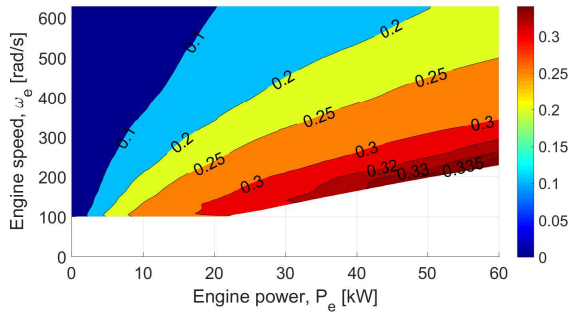

Fig. 9: Efficiency map of the ICE for engine power P_e against engine speed ω_e.

C. Electric Assist Control Strategy

As a commonly used rule-based control strategy, the electric assist control strategy (EACS) [16] uses the ICE as the main power source, and the battery is used to assist the ICE. The EACS operates with the battery when the ICE works inefficiently or the load demand is beyond the ICE maximum power. On the other hand, the ICE produces additional power to charge the battery when the SOC is low. The control rules of the EACS are presented in Fig. 10, where P_{chrg} is the additional power delivered by the ICE to charge the battery in addition to the propulsion load when the SOC value is low

$$P_{chrg} = r_{chrg} \times \left(\frac{SOC_L + SOC_U}{2} - SOC\right) \times \omega_e \qquad (38)$$

with r_{chrg} being a parameter to be tuned, and V_{limit}, r_{min} and r_{off} are three tunable parameters determining the thresholds for the ICE activation. As shown in Fig. 10(b), if the SOC is in the desirable operation region, i.e., $SOC_L \leq SOC \leq SOC_U$, the EACS works with the load-following mechanism.

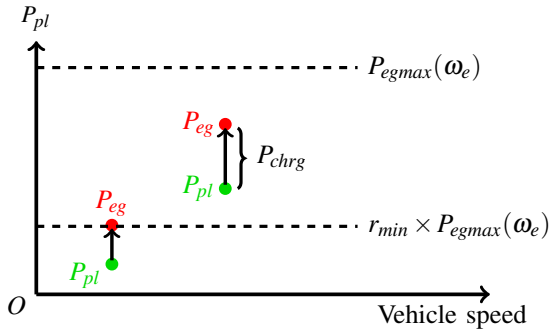

(a) The control strategy behavior for $SOC < SOC_L$.

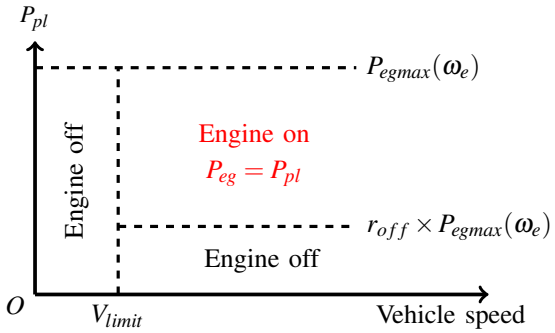

(b) The control strategy behavior for $SOC_L < SOC < SOC_U$.

Fig. 10: The operating modes of the EACS.

Since the lower and upper bounds of the SOC have been fixed in the present work, the EACS has four parameters to be determined, namely, V_{limit}, r_{chrg}, r_{min} and r_{off}. For a fair comparison, the four parameters are tuned by an exhaustive search to minimize the equivalent fuel consumption m_{efc} and are shown in Table V. When simulating WL-L and WL-M, $SOC < SOC_L$ never occurs (operating mode shown in Fig. 10(a)), such that the parameters r_{chrg} and r_{min} will not affect the tuning results and therefore these two parameters can take any value for WL-L and WL-M.

TABLE V: Optimal Parameters in EACS

Driving cycle	V_{limit}	r_{chrg}	r_{min}	r_{off}
WL-L	1.9	any	any	0.19
WL-M	1.8	any	any	0.20
WL-H	1.5	1.4	0.3	0.22
WL-E	2.9	1.5	0.4	0.36

IV. Torque-leveling Threshold-changing Strategy (TTS)

This section derives fundamental design principles for parallel HEV SCSs by review of the general relevant background

in HEV SCSs, and by direct analysis of the ECMS and EACS presented in the previous Section. The aim is to postulate simple rules that capture the most effective control features that are required to operate the HEV powertrain with optimal efficiency, and which are subsequently used to synthesize the new heuristic strategy, TTS.

A. Design principles

1) Torque leveling: In the general context of SCSs, the following arguments hold: 1) With a fixed strategy followed for gear selection, the ICE speed in parallel HEVs varies with the vehicle driving speed, 2) the only degree of freedom available in ICE operation in parallel HEVs is the ICE torque (or power), 3) the most common heuristic strategy for parallel HEVs, the EACS, utilizes the power following approach, but as it will be shown later in Section V it has inferior performance as compared to the ECMS, 4) in series HEVs the power following approach is utilized in PFCS and XOS [3], [19], [20] but it has been shown to have inferior performance than the power leveling approach, exemplified by the OPSS [2], 5) by observing typical ICE efficiency maps, such as the one in Fig. 9, it can be inferred that the power leveling approach is not suitable for parallel HEVs because as the ICE speed increases the ICE efficiency drops significantly along constant power contours, and also at higher power values low ICE speeds are not feasible due to ICE torque saturation, 6) by observing typical ICE efficiency maps, such as the one in Fig. 3, it can be inferred that at a suitably selected constant ICE torque, the ICE efficiency can remain high as the ICE speed varies, 7) by observing exemplary ECMS control maps, such as those in Fig. 8, it can be seen that when the ICE is active it works approximately at constant torque (for a given load demand P_{pl} the power share factor u_{sf} increases with the ICE speed, this is also apparent by comparing with Fig. 12 that will be presented later in Section V). Collectively, these arguments lead to the simplified hypothesis that parallel HEV powertrains will have the best efficiency when operated according to the torque-leveling principle, when the ICE is active.

2) Threshold changing: According to threshold changing operation, predetermined power thresholds are used to activate the ICE, where in the ICE off position the vehicle is powered by the battery only. In the general context of SCSs, the following arguments hold: 1) The threshold changing approach is already used in series HEV SCSs, such as in XOS and OPSS [2], [3], as a more effective and fuel efficient means of enabling charge sustaining operation, as compared to the established state changing approach utilized in TCS and PFCS [19], [20], [22], 2) the threshold changing approach is also present in the series HEV efficiency maximimizing control strategy (EMMS) [34], in which the threshold is SOC dependent, 3) threshold changing operation is also indirectly taking place in the series HEV ECMS [2] when considering drive cycles of different average speeds, 4) the most common SCS for parallel HEVs, the EACS, also utilizes a threshold changing scheme (see Fig. 10), 5) with a fixed strategy followed for gear selection, the ICE speed in parallel HEVs varies with the vehicle driving speed, 6) the ECMS control maps for parallel HEVs, as presented in Fig. 8, also display threshold changing operation, which is engine speed dependent (transition from dark blue to brown colors). These arguments lead to the simplified hypothesis that the most fuel efficient mechanism of charge sustaining operation in parallel HEVs is by threshold changing, in which the power threshold is SOC and ICE-speed dependent.

B. New rule-based control strategy TTS

The two design principles described are used together to develop the novel heuristic control strategy, TTS, for parallel HEVs.

As already presented, the threshold changing mechanism in parallel HEVs needs to have a more elaborate form that depends on both the SOC and ICE speed, in contrast to the SOC-dependent only power threshold employed in series HEVs. Therefore, the power threshold is defined in the present work as:

$$\begin{aligned} P_{egmin}(SOC,\omega_e) &\triangleq P_{th}+P_{th}\frac{SOC-SOC_{mid}}{SOC_{range}}+P_{\omega}+P_{\omega}\frac{\omega_e-\omega_{mid}}{\omega_{range}} \\ &= P_{th}\frac{SOC-SOC_L}{SOC_{range}}+P_{\omega}\frac{\omega_e-\omega_L}{\omega_{range}}, \end{aligned} \tag{39}$$

where P_{th} is the power threshold related to SOC, P_{ω} adjusts the power threshold by considering the ICE speed, and

$$X_{mid} \triangleq \frac{X_U+X_L}{2},\ X_{range} \triangleq \frac{X_U-X_L}{2}$$

with $X \in \{SOC, \omega\}$. By using the proposed SOC and ICE-speed dependent threshold (39), the TTS is not only able to ensure a charge-sustaining operation, but it can also avoid inefficient operations of the ICE.

The operating rules of the TTS are shown in Fig. 11. Since a 3-dimensional representation in terms of SOC, ω_e and P_{pl} is required, for presentation purposes only two cross sections at $\omega_e = \omega_{mid}$ and $SOC = SOC_{mid}$ of the overall representation are depicted. T_{eg} $(= P_{eg}/\omega_e)$ represents the output torque of the primary source.

The SOC dependence of the threshold is presented in Fig. 11(a), which governs the activation of the ICE when $SOC \geq SOC_L$ and it is analogous to the one presented in the XOS and OPSS for series HEVs [2], [3]. Fig. 11(b) shows that the proposed TTS is designed to have an analogous threshold changing feature to the control maps produced by the ECMS (see Fig. 8), which will activate the ICE at a higher load demand for a higher engine speed (diagonal line between yellow and green areas with one end at point $(P_{th},\ \omega_L)$). Furthermore, the TTS applies the torque-leveling approach when the ICE is active as shown in both Figs. 11(a) and 11(b), which operates the primary source with a constant torque T_c (green areas). In contrast to the DP and ECMS that need to solve sophisticated optimization problems, the TTS is synthesized by simple rules with only three parameters, T_c, P_{th}, P_{ω}, which can be determined by minimizing the equivalent fuel consumption m_{efc} defined in Section V-C, and which largely capture the features of the ECMS control maps.

By minimizing the equivalent fuel consumption m_{efc}, the optimal values for the three parameters of the TTS for different

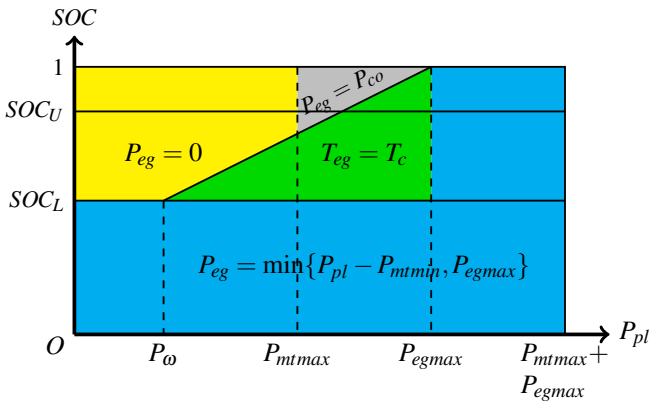

(a) The cross section of control rules at $\omega_e=\omega_{mid}$.

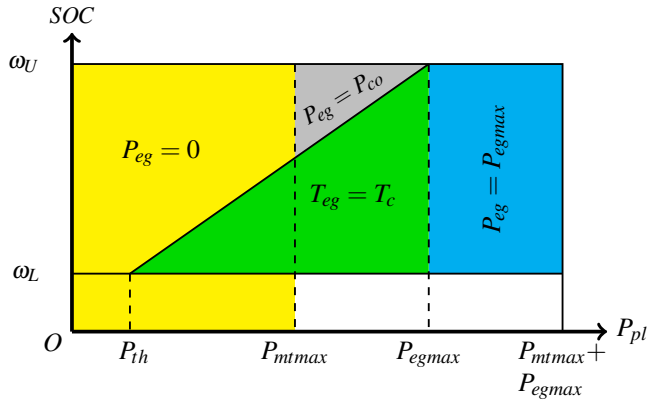

(b) The cross section of control rules at $SOC=SOC_{mid}$.

Fig. 11: The TTS operates in four modes depending on the given SOC, ω_e and P_{pl}: Battery mode (yellow), constant ICE torque mode (green), maximum ICE power mode (blue), and maximum secondary source power mode (gray) with $P_{co} \triangleq P_{pl}-P_{mtmax}$. White represents the infeasible region.

driving cycles can be obtained via an exhaustive search, and are presented in Table VI.

TABLE VI: Optimal Parameters in TTS

Driving cycle	P_{th}	P_ω	T_c
WL-L	7.0	11.0	143
WL-M	6.2	15.6	144
WL-H	2.0	17.2	146
WL-E	9.6	23.0	151

For illustration purposes, the cross sections of the control maps of the TTS with the corresponding optimized parameters for different drive cycles are presented in Fig. 12. It can be seen that the cross sections with the fixed SOC value of $SOC=SOC_{mid}$ (corresponding to plots in the second row of Fig. 12) have similar patterns as the control maps produced by the ECMS as presented in Fig. 8, which may imply the effectiveness of the proposed TTS.

C. Simplified TTS (STTS)

By inspection of the control rules in Fig. 11(b), it is obvious that the importance of the parameter P_ω in the TTS, which defines the slope of the diagonal line, depends on the variation of ICE speed, ω_e, during a driving cycle. If this variation is small, which may be true in practice, P_ω can be ignored for simplicity ($P_\omega=0$) and the following ICE activation threshold can be used instead:

$$P_{egmin}(SOC)=P_{th}+P_{th}\frac{SOC-SOC_{mid}}{SOC_{range}}. \tag{40}$$

Thus, the heuristic control rules are simplified from a 3D to 2D set of rules, with the complete representation given by Fig. 11(a), which has the same (SOC-dependent only) threshold changing scheme as the XOS and OPSS for series HEV in [2], [3] but uses the torque leveling approach to ensure the fuel efficiency. The STTS has only two parameters (P_{th} and T_c) to tune.

Similarly to the TTS, the two optimized parameters in the STTS are obtained by an exhaustive search to minimize the equivalent fuel consumption m_{efc} and are presented in Table VII for different driving cycles.

TABLE VII: Optimal Parameters in Simplified STTS

Driving cycle	P_{th}	T_c
WL-L	10.4	142
WL-M	14.8	146
WL-H	13.4	146
WL-E	38.4	151

To highlight the advantages of the TTS (and STTS), various comparisons of features with conventional control strategies are summarized in Table VIII.

V. Simulation Results

The SCSs presented in Sections III (DP and EACS) and IV (TTS and STTS) are now implemented to the constructed vehicle model (33) and simulated to investigate their operation and performance, and thus the effectiveness of the proposed heuristic strategy will be evaluated. In the present work in which the vehicle model is relatively simple, since the DP and ECMS achieve similar performance, the simulation results for the ECMS are omitted for conciseness purposes. The DP results (the global optimal solution) are presented to benchmark the heuristic control strategies. Simulation are performed for the four component driving cycles of the worldwide harmonized light vehicles test procedure (WLTP): WL-L (low speed), WL-M (medium speed), WL-H (high speed) and WL-E (extra-high speed), as shown in Fig. 13. These driving speed profiles have recently been designed by the EU automobile industry and the United Nations employing real-driving and worldwide-gathered data, to represent more accurately real-world driving conditions in comparison to older driving cycles, and to serve as a global standard for the measurement of emissions, fuel consumption and electric range of light-duty vehicles [35]. Also, under EU law, this specification has been selected for passenger cars lab testing to succeed the now outdated New European Driving Cycle (NEDC).

A. Power Profiles

1) DP: It can be seen from Fig. 14 that pure electric operations are activated at low power loads and that the ICE

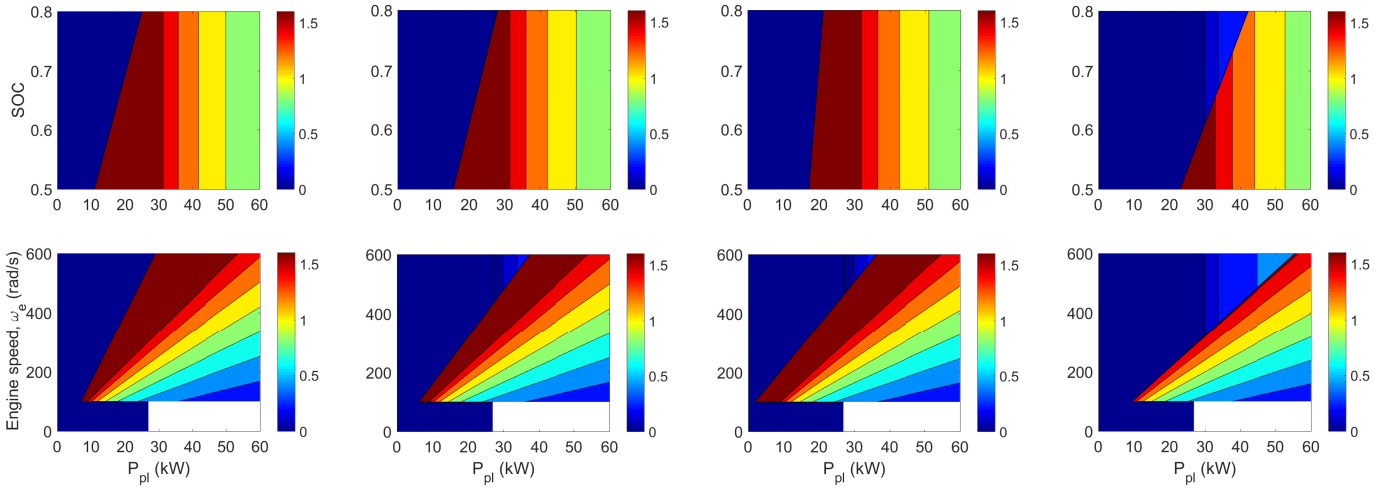

(a) WL-L (b) WL-M (c) WL-H (d) WL-E

Fig. 12: The cross sections at $\omega_e = \omega_{mid}$ (top) and $SOC = SOC_{mid}$ (bottom) of the control maps ($u_{sf} = P_{eg}/P_{pl}$) with the optimized parameters (as shown in Table VI) for drive cycles WL-L, WL-M, WL-H and WL-E, respectively. Dark blue corresponds to pure electric mode and white represents the infeasible region.

TABLE VIII: Comparison of different control strategies

	TTS	DP	ECMS	EACS
type	rule-based	optimization-based	optimization-based	rule-based
applicable vehicle models	any complex model	one-state model	any complex model (but optimality weakens with model complexity)	any complex model
real-time implementation	easy	not easy	not easy	easy
number of tuning parameter	3 (2 for STTS)	N.A.	2	4
tuning time	$\frac{1}{2}$ of ECMS tuning time ($\frac{1}{3}$ of ECMS tuning time for STTS)	N.A.	ECMS	$\frac{2}{3}$ of ECMS tuning time
ICE operating efficiency	nearly optimized	optimized	optimized	not optimized
charge sustainability	yes	yes	yes	no

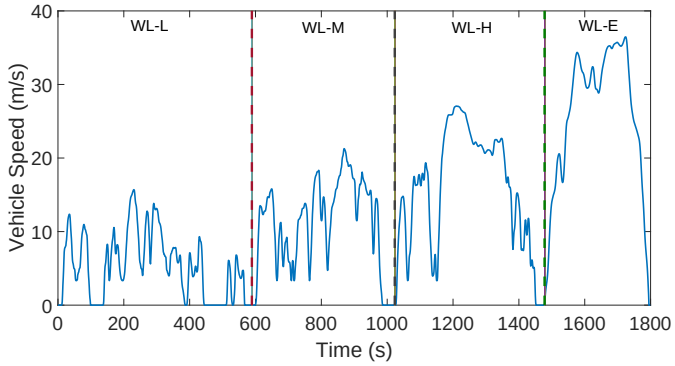

Fig. 13: Speed profile of the WLTP with four different stages (WL-L, WL-M, WL-H and WL-E).

is switched on at operating points with high propulsion loads. Also, once the ICE is activated, it usually delivers more power than the propulsion load, and the excess power is stored into the battery for future use. This can not only maintain the SOC level, but also ensure that the ICE works in an efficient operating region. For WL-L and WL-M, the DP can be characterized by frequent switching of the primary source, while this source works for no more than 20 s when activated. In the case of WL-H and WL-E, the DP performs somewhat more continuous operation due to the high power demand. It is worth noting that for the presented vehicle model, the DP rarely operates with a hybrid mode that drives the vehicle by using the ICE and battery simultaneously.

2) EACS: The power profiles of the EACS for different driving cycles are presented in Fig. 15, from which it is easy to observe the load-following feature of the EACS. For WL-L and WL-M, it can be seen that in terms of the activation times of the ICE, the EACS has a similar performance with the DP. However, due to the load-following mechanism, the ICE may not work efficiently when active, which would lead to a worse fuel economy in the EACS. For WL-H and WL-E, it is evident that the EACS activates the ICE more frequently than the DP does and that the load-following mechanism is violated during the time intervals $[250, 330]$ s in WL-H and $[70, 250]$ s in WL-E, since the lower bound SOC_L of the SOC might be reached during these time intervals which triggers the activation of the ICE and encourages to use the ICE to recharge the battery. As compared to the DP, the frequent activation of the ICE may also cause a sacrifice in fuel economy.

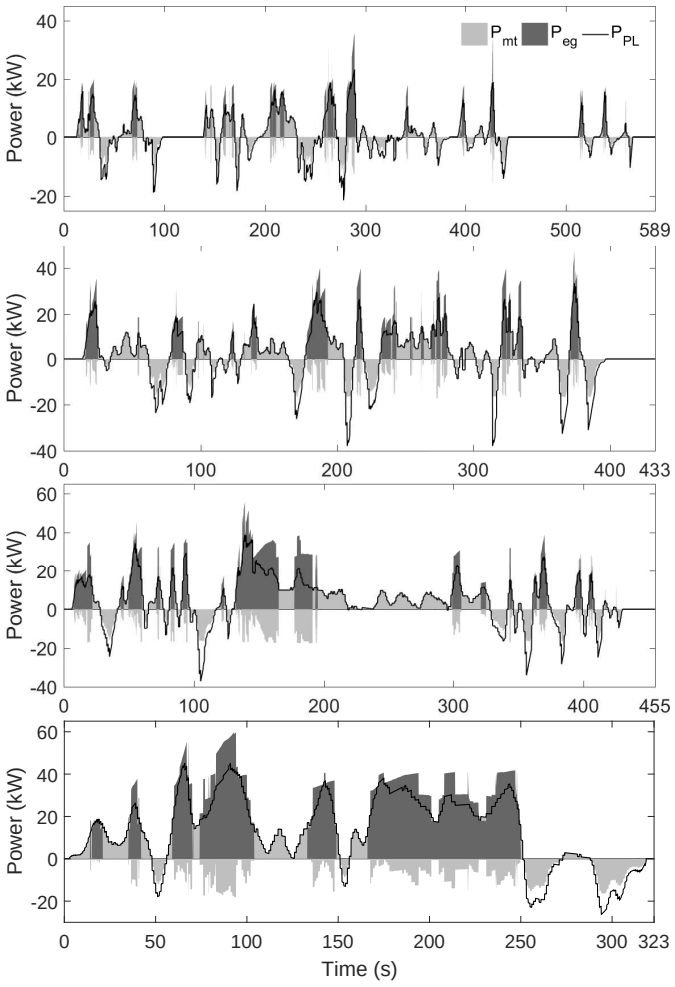

Fig. 14: Power time histories for the primary source (P_{eg}), secondary source (P_{mt}) and power demand (P_{pl}) for the driving cycles WL-L, WL-M, WL-H and WL-E (top to bottom) with DP. The white gap between P_{pl} and P_{mt} represents mechanical brakes.

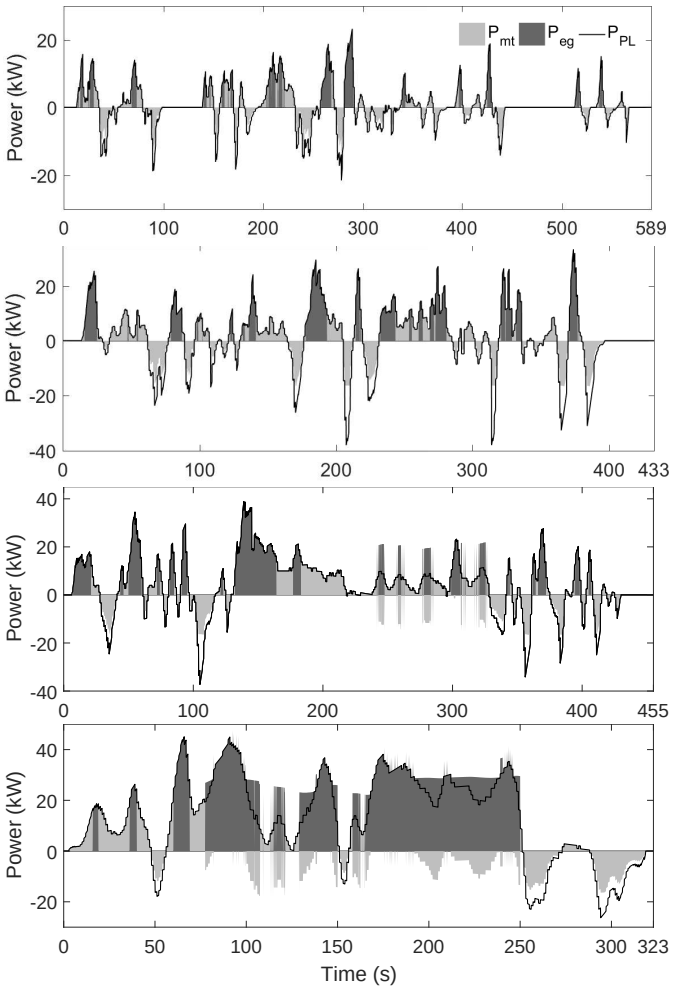

Fig. 15: Power time histories for the primary source (P_{eg}), secondary source (P_{mt}) and power demand (P_{pl}) for the driving cycles WL-L, WL-M, WL-H and WL-E (top to bottom) with EACS. The white gap between P_{pl} and P_{mt} represents mechanical brakes.

3) TTS: The resulting power profiles of the TTS with different drive cycles are shown in Fig. 16. It can be seen that, with the torque-leveling mechanism, the TTS usually operates the ICE to charge the battery once it is activated, which is similar to the operation of DP. Moreover, by comparing Figs. 14 and 16 it is evident that the operations of the TTS and the DP for WL-L and WL-M are very similar in terms of the activation occasions of the ICE. In contrast to the DP, the TTS has shorter ICE activation durations but larger ICE power magnitudes. However, the differences between the DP and TTS become more obvious when driving WL-H and WL-E. The TTS operates the ICE steadily when active, while the DP operates the ICE with more variations in power levels. Additionally, as compared to the DP the TTS activates the ICE more frequently when driving WL-H and WL-E during the time intervals $[200, 300]$ s and $[100, 250]$ s respectively. Moreover, in contrast to the DP the hybrid mode is visible in the TTS when driving WL-E in the time interval $[50, 100]$ s.

4) STTS: The resulting power split profiles of the STTS for the four different drive cycles are presented in Fig. 17. It is obvious that the operation of the STTS is very similar to the TTS for WL-L and WL-M. For WL-H and WL-E, the STTS operates the ICE with more frequent switching, as the threshold becomes smaller by setting $P_{\omega} = 0$. When the ICE is active, the power magnitudes of respectively the ICE and battery for the TTS and STTS are almost the same. However, the frequent switching of the ICE at lower loads by the STTS may lead to a sacrifice of fuel economy.

B. State of Charge Profiles

Besides the power split profiles, the SOC profiles of the four control strategies investigated are presented in Fig. 18 for four driving cycles. It is shown that for the DP and TTS, the charge is sustained for all the drive cycles. Additionally, the DP and TTS SOC profiles are quite steady, as influenced by the efficiency characteristics of the secondary source (see Fig. 5); optimal operation is achieved when the SOC is

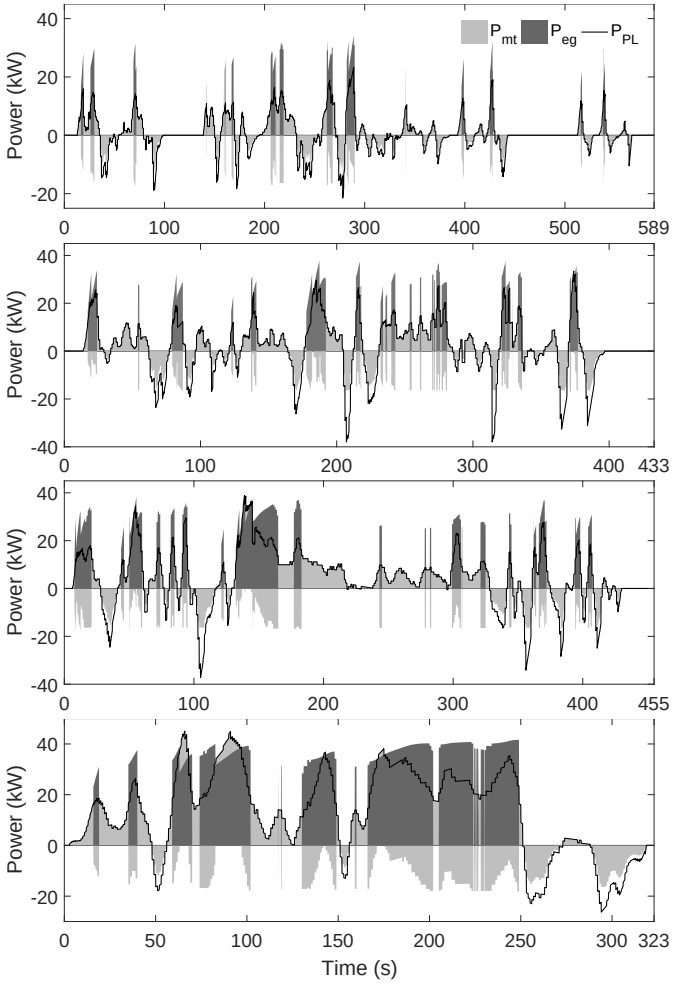

Fig. 16: Power time histories for the primary source (P_{eg}), secondary source (P_{mt}) and power demand (P_{pl}) for the driving cycles WL-L, WL-M, WL-H and WL-E (top to bottom) with TTS. The white gap between P_{pl} and P_{mt} represents mechanical brakes.

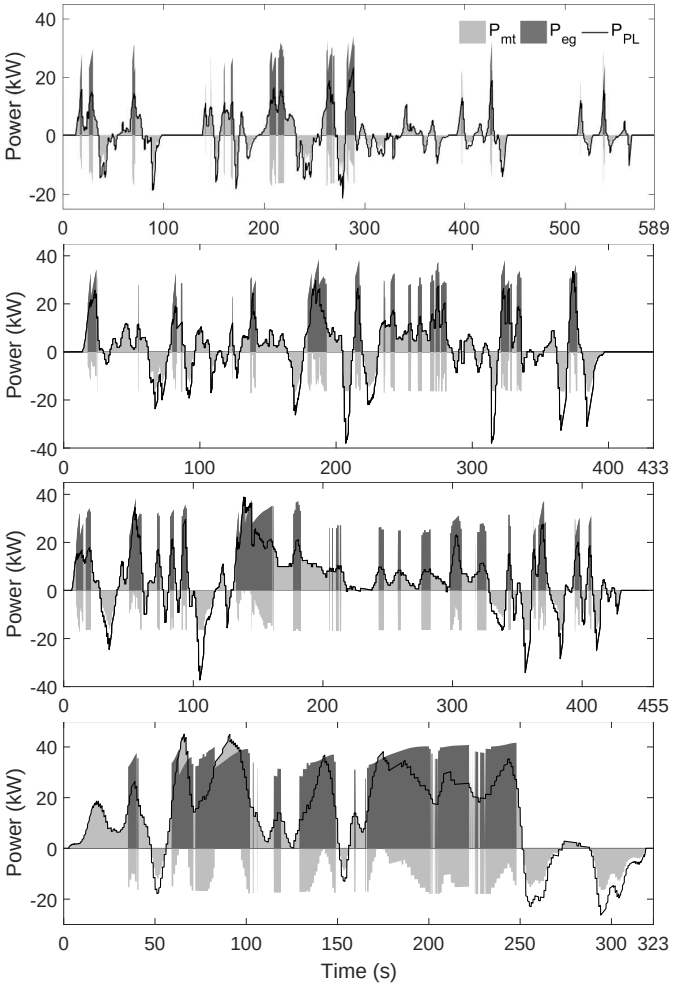

Fig. 17: Power time histories for the primary source (P_{eg}), secondary source (P_{mt}) and power demand (P_{pl}) for the driving cycles WL-L, WL-M, WL-H and WL-E (top to bottom) with STTS. The white gap between P_{pl} and P_{mt} represents mechanical brakes.

discouraged from falling during discharging and rising during charging, overall seen as a lower variation of SOC from the desired value of 0.65 as compared to the EACS. The efficiency characteristics of the secondary source also imply that a SOC-dependent threshold, as utilized in the TTS (see (39)), is beneficial for optimal operation. Thus, the SOC-dependent threshold in TTS helps to maintain steady SOC profiles, similarly to the globally optimal solutions of DP. Similar phenomena can also be observed for STTS when following different driving cycles. The similarity of the SOC profiles between the proposed heuristic strategies and the DP thus also reflects the effectiveness of the TTS and STTS. However, for the EACS the charge-sustaining operation cannot be achieved for all the drive cycles due to the load following mechanism and the limited amount of regenerative braking, whereby the lower bound of the SOC is reached in both the WL-H and WL-E. Therefore, from a charge-sustaining point of view, the proposed TTS and STTS can achieve similar results as the DP and significantly outperform the EACS.

C. Fuel Economy

Due to the difficulty of achieving exact charge-sustaining operation for different SCSs, a uniform evaluation rule for both the fuel and charge consumption is employed to assess the control strategies [36]:

$$m_{efc} = \begin{cases} m_f + S_{d,efc}\Delta SOC\frac{Q_{max}V_{b,OC}}{Q_{LHV}} & \Delta SOC \geq 0 \\ m_f + S_{c,efc}\Delta SOC\frac{Q_{max}V_{b,OC}}{Q_{LHV}} & \Delta SOC < 0 \end{cases}, \qquad (41)$$

where $\Delta SOC = SOC_{initial} - SOC_{final}$, $S_{d,efc}$ and $S_{c,efc}$ are two equivalence factors. Similarly to [2], [36], this work applies the line-chart approach to determine the equivalence factors between SOC and real fuel consumption, which are given in Table IX and will be used to evaluated the fuel economy of different control strategies.

The resulting fuel economies of the four control strategies are presented for the four driving cycles respectively in Tables X-XIII. The first rows in each table display the actual fuel consumption, the second rows show the final SOC values, and the third rows use the first two rows in each case and (41), and

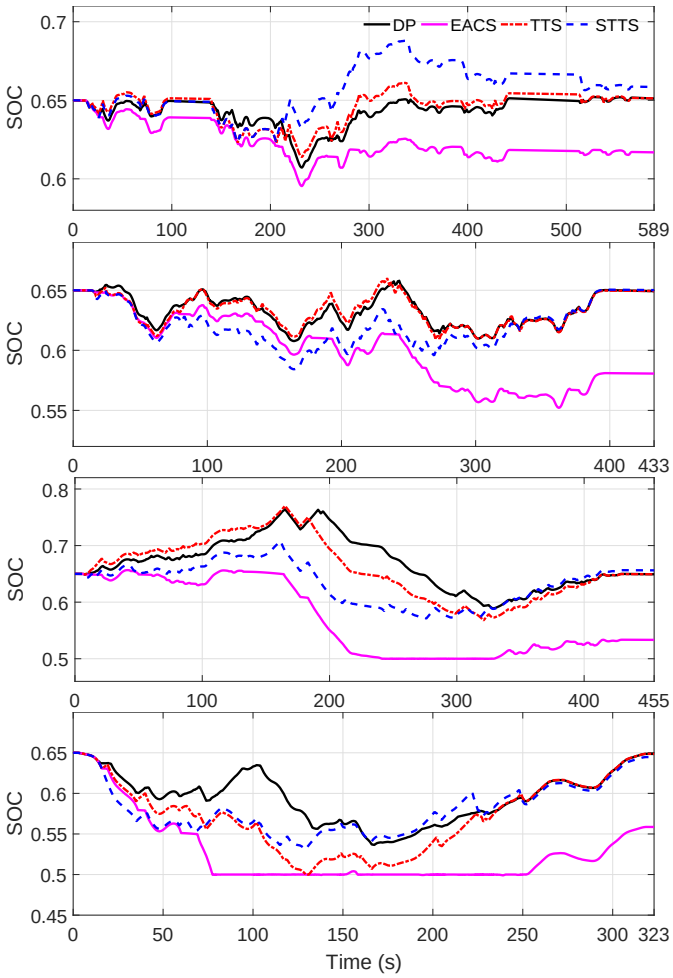

Fig. 18: SOC profiles of DP, EACS, TTS, and STTS for the driving cycles WL-L, WL-M, WL-H and WL-E (top to bottom).

TABLE IX: Equivalent Fuel Consumption Factors

Drive cycle	$S_{d,efc}$	$S_{c,efc}$
WL-L	4.40	3.77
WL-M	4.26	3.28
WL-H	3.70	3.12
WL-E	3.13	2.03

calculate the corresponding equivalent fuel consumption m_{efc}. The last rows of the tables give the relative equivalent fuel consumption performance of each control strategy with respect to the equivalent fuel consumption of the DP. The comparative equivalent fuel consumption results are also illustrated in Fig. 19.

TABLE X: Comparison of Fuel Economy for WL-L.

	EACS	TTS	STTS	DP
Fuel [kg]	0.0864	0.0949	0.0989	0.0923
SOC_{final}	0.6169	0.6512	0.6585	0.6511
m_{efc} [kg]	0.1016	0.0944	0.0956	0.0928
Δm_{efc} [%]	+10.08	+2.28	+3.58	+0

From Tables X-XIII, it can be seen that the fuel economy of the EACS is not great and that its equivalent fuel consumption

TABLE XI: Comparison of Fuel Economy for WL-M.

	EACS	TTS	STTS	DP
Fuel [kg]	0.1422	0.1596	0.1614	0.1577
SOC_{final}	0.5806	0.6493	0.6501	0.6493
m_{efc} [kg]	0.1733	0.1599	0.1614	0.1581
Δm_{efc} [%]	+9.61	+1.14	+2.09	+0

TABLE XII: Comparison of Fuel Economy for WL-H.

	EACS	TTS	STTS	DP
Fuel [kg]	0.2258	0.2586	0.2667	0.2534
SOC_{final}	0.5333	0.6494	0.6562	0.6493
m_{efc} [kg]	0.2711	0.2588	0.2646	0.2537
Δm_{efc} [%]	+6.86	+2.01	+4.30	+0

TABLE XIII: Comparison of Fuel Economy for WL-E.

	EACS	TTS	STTS	DP
Fuel [kg]	0.3902	0.4122	0.4150	0.4068
SOC_{final}	0.5586	0.6487	0.6447	0.6486
m_{efc} [kg]	0.4203	0.4127	0.4167	0.4073
Δm_{efc} [%]	+3.19	+1.33	+2.31	+0

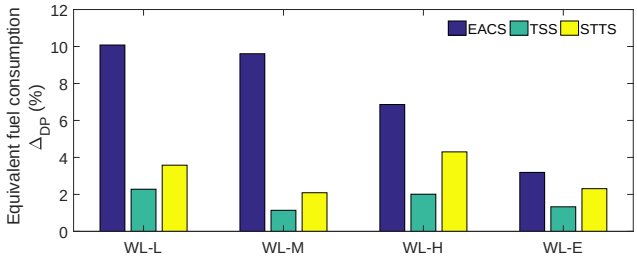

Fig. 19: Comparison of equivalent fuel consumption for the EACS, TTS and STTS relative to the performance of the DP, when driving the WL-L, WL-M, WL-H and WL-E.

lags the DP results by 3.19%-10.08%, with a combined difference (considering the four driving cycles together) of 6.02%. The performance of the TTS is much better than the EACS in terms of both the fuel economy and the charge-sustaining operation. It is found that the TTS is able to achieve a great fuel economy, which only lags the DP by 1.14%-2.28%. If the four driving cycles are considered together, the difference is only 1.58%. Given the simple rules and easy tuning procedures of the TTS, its performance is impressive, while it is easy to implement it to any complex vehicle model, which might be difficult or impossible with DP and other optimization based control strategies, such as ECMS. The STTS lags the DP by 2.09%-4.30% in terms of fuel economy, with a combined difference of 2.95%. Therefore, with a relatively small sacrifice of fuel economy as compared to the TTS but with still significantly better fuel economy than EACS, the STTS saves more than one third of the tuning effort when compared with the TTS and it is also more convenient for real-time implementation with only two parameters to be adapted.

VI. CONCLUSION

Inspired by the most effective features of various existing heuristic and optimization-based control strategies for fuel efficient operation of both series and parallel hybrid electric vehicles (HEVs), this work develops a novel rule-based control

strategy for parallel HEVs: the torque-leveling threshold-changing strategy (TTS). The TTS employs the newly introduced torque leveling approach together with a threshold-changing mechanism enhanced from its previous applications in series HEVs. The main operating rules are as follows: the powertrain operates in pure electric mode at low power demands; the powertrain enters hybrid operation with the ICE operating with a constant torque at medium power demands; the low and medium power demands are distinguished by a battery charge and engine speed dependent threshold; and the ICE operates at its maximum power at higher loads or when the battery charge falls below a lower threshold. Even though the TTS is formulated by simple rules (parameterized by only three tuning parameters) and easy tuning procedures, it produces an impressive fuel economy performance that lags the global optimal solutions of dynamic programming (DP) only by 1.58%, and outperforms the conventional electric assist control strategy (EACS) by 5.04%, while achieving charge-sustaining operation similar to DP. From an implementation point of view, the TTS outperforms the DP as it can easily be implemented to any complex vehicle model for which DP might be unsolvable. A simplified version of the TTS (STTS) with only two tuning parameters is also provided, which is able to deliver almost similar performance to the TTS but which is more convenient to be implemented in practice.

REFERENCES

[1] M. Sabri, K. Danapalasingam, and M. Rahmat, "A review on hybrid electric vehicles architecture and energy management strategies," *Renewable and Sustainable Energy Reviews*, vol. 53, pp. 1433–1442, 2016.

[2] W. Shabbir, "Control strategies for series hybrid electric vehicles," 2015.

[3] W. Shabbir and S. A. Evangelou, "Exclusive operation strategy for the supervisory control of series hybrid electric vehicles," *IEEE Transactions on Control Systems Technology*, vol. 24, no. 6, pp. 2190–2198, 2016.

[4] C. Hou, M. Ouyang, L. Xu, and H. Wang, "Approximate pontryagins minimum principle applied to the energy management of plug-in hybrid electric vehicles," *Applied Energy*, vol. 115, pp. 174–189, 2014.

[5] S. Di Cairano, W. Liang, I. V. Kolmanovsky, M. L. Kuang, and A. M. Phillips, "Power smoothing energy management and its application to a series hybrid powertrain," *IEEE Transactions on control systems technology*, vol. 21, no. 6, pp. 2091–2103, 2013.

[6] T. Liu, X. Hu, S. E. Li, and D. Cao, "Reinforcement learning optimized look-ahead energy management of a parallel hybrid electric vehicle," *IEEE/ASME Transactions on Mechatronics*, vol. 22, no. 4, pp. 1497–1507, 2017.

[7] X. Zeng and J. Wang, "A parallel hybrid electric vehicle energy management strategy using stochastic model predictive control with road grade preview," *IEEE Transactions on Control Systems Technology*, vol. 23, no. 6, pp. 2416–2423, 2015.

[8] C. Pisanti, G. Rizzo, and V. Marano, "Energy management of through-the-road parallel hybrid vehicles," *IFAC Proceedings Volumes*, vol. 47, no. 3, pp. 2118–2124, 2014.

[9] C.-C. Lin, H. Peng, J. W. Grizzle, and J.-M. Kang, "Power management strategy for a parallel hybrid electric truck," *IEEE transactions on control systems technology*, vol. 11, no. 6, pp. 839–849, 2003.

[10] G. Paganelli, S. Delprat, T.-M. Guerra, J. Rimaux, and J.-J. Santin, "Equivalent consumption minimization strategy for parallel hybrid powertrains," in *IEEE 55th Vehicular Technology Conference*, vol. 4, 2002, pp. 2076–2081.

[11] L. Serrao, S. Onori, and G. Rizzoni, "Ecms as a realization of pontryagin's minimum principle for hev control," in *American Control Conference*, 2009, pp. 3964–3969.

[12] B. Geng, J. K. Mills, and D. Sun, "Energy management control of microturbine-powered plug-in hybrid electric vehicles using the telemetry equivalent consumption minimization strategy," *IEEE transactions on Vehicular Technology*, vol. 60, no. 9, pp. 4238–4248, 2011.

[13] C. Musardo, G. Rizzoni, Y. Guezennec, and B. Staccia, "A-ecms: An adaptive algorithm for hybrid electric vehicle energy management," *European Journal of Control*, vol. 11, no. 4-5, pp. 509–524, 2005.

[14] A. Panday and H. O. Bansal, "Energy management strategy implementation for hybrid electric vehicles using genetic algorithm tuned pontryagins minimum principle controller," *International Journal of Vehicular Technology*, vol. 2016, 2016.

[15] S. G. Wirasingha and A. Emadi, "Classification and review of control strategies for plug-in hybrid electric vehicles," *IEEE Transactions on vehicular technology*, vol. 60, no. 1, pp. 111–122, 2011.

[16] M. Montazeri-Gh, A. Poursamad, and B. Ghalichi, "Application of genetic algorithm for optimization of control strategy in parallel hybrid electric vehicles," *Journal of the Franklin Institute*, vol. 343, no. 4-5, pp. 420–435, 2006.

[17] V. H. Johnson, K. B. Wipke, and D. J. Rausen, "Hev control strategy for real-time optimization of fuel economy and emissions," SAE Technical Paper, Tech. Rep., 2000.

[18] M. Delkhosh, M. S. Foumani, and P. Rostami, "Optimization of power train and control strategy of hybrid electric vehicles," *Scientia Iranica. Transaction B, Mechanical Engineering*, vol. 22, no. 5, p. 1842, 2015.

[19] N. Jalil, N. A. Kheir, and M. Salman, "A rule-based energy management strategy for a series hybrid vehicle," in *American Control Conference*, vol. 1, 1997, pp. 689–693.

[20] M. R. Cuddy and K. B. Wipke, "Analysis of the fuel economy benefit of drivetrain hybridization," National Renewable Energy Lab., Golden, CO (US), Tech. Rep., 1997.

[21] C. Anderson and E. Pettit, "The effects of apu characteristics on the design of hybrid control strategies for hybrid electric vehicles," SAE Technical Paper, Tech. Rep., 1995.

[22] C. G. Hochgraf, M. J. Ryan, and H. L. Wiegman, "Engine control strategy for a series hybrid electric vehicle incorporating load-leveling and computer controlled energy management," SAE Technical Paper, Tech. Rep., 1996.

[23] J. Van Mierlo and G. Maggetto, "Views on hybrid drivetrain power management strategies," *Proceedings of the EVS-17, Montreal, Canada*, 2000.

[24] T. Knoke, C. Romaus, and J. Böcker, "Optimization and comparison of heuristic control strategies for parallel hybrid-electric vehicles," in *Electric Vehicle Symposium*, vol. 23. Citeseer, 2005.

[25] L. Serrao, S. Onori, and G. Rizzoni, "A comparative analysis of energy management strategies for hybrid electric vehicles," *Journal of Dynamic Systems, Measurement, and Control*, vol. 133, no. 3, p. 031012, 2011.

[26] https://ricardo.com/software/products/wave.

[27] O. Tremblay and L.-A. Dessaint, "Experimental validation of a battery dynamic model for ev applications," *World Electric Vehicle Journal*, vol. 3, no. 1, pp. 1–10, 2009.

[28] P. Pillay and R. Krishnan, "Modeling, simulation, and analysis of permanent-magnet motor drives," *IEEE Transactions on industry applications*, vol. 25, no. 2, pp. 265–273, 1989.

[29] S. A. Evangelou and W. Shabbir, "Dynamic modeling platform for series hybrid electric vehicles," *IFAC-PapersOnLine*, vol. 49, no. 11, pp. 533–540, 2016.

[30] R. Lot and S. A. Evangelou, "Green driving optimization of a series hybrid electric vehicle," in *IEEE 52nd Annual Conference on Decision and Control (CDC)*, 2013, pp. 2200–2207.

[31] S. A. Evangelou and A. Shukla, "Advances in the modelling and control of series hybrid electric vehicles," in *Proceedings of American Control Conference*, 2012.

[32] M. Guiggiani, *The science of vehicle dynamics: handling, braking, and ride of road and race cars*. Springer Science & Business Media, 2014.

[33] O. Sundstrom and L. Guzzella, "A generic dynamic programming matlab function," in *IEEE Control Applications,(CCA) & Intelligent Control (ISIC)*, 2009, pp. 1625–1630.

[34] W. Shabbir and S. A. Evangelou, "Real-time control strategy to maximize hybrid electric vehicle powertrain efficiency," *Applied energy*, vol. 135, pp. 512–522, 2014.

[35] P. Mock, J. Kuhlwein, U. Tietge, V. Franco, A. Bandivadekar, and J. German, "The wltp: How a new test procedure for cars will affect fuel consumption values in the eu," *The International Council on Clean Transportation*, 2014.

[36] A. Sciarretta, M. Back, and L. Guzzella, "Optimal control of parallel hybrid electric vehicles," *IEEE Transactions on control systems technology*, vol. 12, no. 3, pp. 352–363, 2004.